

Katja Friedrich<sup>+</sup>, David Kingsmill<sup>+</sup>, and Carl Young<sup>\* \*</sup>  
<sup>+</sup> University of Colorado, CIRES, Boulder, Colorado  
<sup>\*</sup> Desert Research Institute, Reno, Nevada

## 1. INTRODUCTION

Convection initiation often occurs non-uniformly along boundary layer convergence lines, such as gust fronts, which leads to difficulties in accurate nowcasting of severe local storms. Besides regional variations in thermodynamic stability, kinematic variability linked to horizontal shear instabilities can produce wave pattern that produce small scale (<4 km) vertical vorticity maxima referred to as misocyclones (Fujita 1981). Misocyclone development induced by horizontal shearing instabilities is one manifestation of kinematic variability along such boundaries that may have an impact on convection initiation. However, a clear link between convection initiation and misocyclone development along boundaries has not yet been verified either through observations or numerical simulations.

Early works going back to ? investigating the relationship between land-sea breeze associated with the initiation of deep convection along the Florida Peninsula using a network of anemometers. Since then initiation of convection at boundary-layer convergence have been intensively investigated both along the Florida Peninsula, see for instance Cooper et al. (1982); Watson and Blanchard (1984) and references therein, the region east of the Colorado Rocky Mountains near Denver Wilson and Schreiber (1986), or in the eastern United States Purdom and Marcus (1982) using primarily Doppler radar observations.

Although the knowledge about processes leading to severe storm outbreaks have been investigated over the last years, little is known about misocyclone development along lower-tropospheric boundaries and its relationship to convection initiation. Furthermore, the relationship between misocyclones and convective initiations has not yet been fully proved by both numerical simulations and observations.

During the Convection and Precipitation/Electrification (CaPE) experiment conducted in east-central Florida during July-August 1991, a series of misocyclones spaced at 3-5 km intervals were observed along an intense gust front (Kingsmill 1995). Although convergence and vertical velocity maxima were observed at locations adjacent to each of the misocyclones, they were not preferred areas of convection development. In contrast, results from numerical simulations of thunderstorm outflows indicate that misocyclone locations and their associated regions of convergence and vertical velocity maxima were indeed preferred areas of convection development (Lee and Wilhelmson 1997).

Since fundamentally different conclusions regarding the importance of horizontal shearing instabilities in convection

initiation exist, this study focuses on a broader analysis of kinematic structures along gust fronts observed during CaPE.

## 2. OBSERVATIONS

For the investigation of kinematic structures associated with the development of horizontal shearing instabilities along thunderstorm outflow, observations were analyzed which were collected during the Convection and precipitation/Electrification (CaPE) experiments at east-central Florida near Cape Canaveral during July and August 1991. More information on the CaPE experiment, data sources, and results of case studies can be found for instance in Atkins et al. (1995); Frankhauser et al. (1995); Laird et al. (1995); Kingsmill (1995); Wakimoto and Kingsmill (1995); Yuter and Houze (1995) and references therein. For more information on bore formation from colliding density currents during CaPE, authors refer to Kingsmill and Crook (2003). The observational systems used for this investigation consist of the C-band Doppler radar systems, CP3 and CP4, operated by the National Center for Atmospheric Research (NCAR), and the Federal Aviation Administration-sponsored FL2. The distances between the radars ranged from 23.2 km for CP3-CP4, 38.3 km for CP3-FL2 until 59.2 km for CP4-FL2. The investigation was limited to eleven cases where gust fronts passed the investigation area while at least two radar systems were in operation. Location of the gust front together with the radar systems in operation are illustrated schematically in Fig. 1. In order to investigate

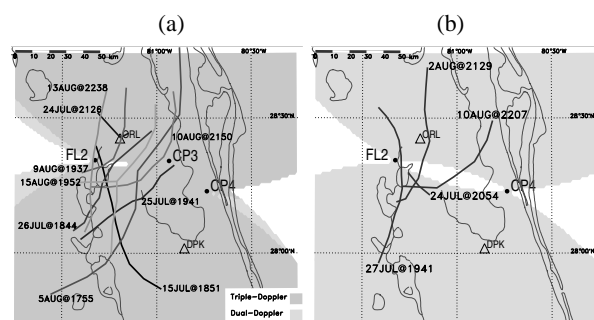


FIG. 1: Map of the investigation area for (a) a three Doppler radar performance and (b) a two radar performance during the CaPE field experiment in Florida. Location of radars (CP2, CP3, and FL2); the radiosounding sites at Orlando (ORL) and at Deer Park (DPK); and the position of the gust fronts are illustrated for the eleven cases included in the analysis. The location of the gust front represents the first time step to be analyzed. Note that both on 24 July and 10 August 1991, the CP3 radar system was only temporarily in operation.

<sup>\*</sup> Corresponding author address: Katja Friedrich, CIRES, 216 UCB, Boulder, CO 80309-0216; e-mail: katja.friedrich@noaa.gov

low-level convergence and vorticity structures that influence the organization and development of severe storms, radar observations at  $0.3^\circ$  elevation are utilized. Since only the lowest elevation level is used, the wind synthesis is restricted to determine solely the horizontal wind vector. The linear system of equations to calculate the horizontal wind components  $u$ ,  $v$  is determined exactly in areas labeled as dual-Doppler and overdetermined in triple-Doppler areas (Fig. 1). Table 1 gives an overview about each case showing the number of radars in operation, the number of low-level scans included in the analysis, the length of the analyzed gust front, and characteristics of the gust front itself like propagation speed and direction. The dual-Doppler performance consists always of radars CP4 and FL2 (Fig. 1b). For the wind analysis, time differences between each radar's low-level scan were chosen to be below one minute, while always the closes available time steps was chosen. This means, although more volume scans were performed by each individual radar, the time difference to the other radar scans was too large. The difference between two successive analysis time steps varies between 5 minutes (e.g. 13 Aug) up to 30 minutes (e.g. 24 Jul) with an average of about 15 minutes.

Table 1: Analysis parameters and pre-collision characteristics of the gust-front: number of analysis times (# time), number of Doppler radars for wind analysis (# radars), average analysed gust-front length  $\Delta y'$ , propagation speed and direction  $\overline{UP_{SPD}}$ ,  $\overline{UP_{DIR}}$ . Cases with convective cell initiation after the gust front passage are highlighted in bold.

Date	# time	# radars	$\Delta y'$ (km)	$\overline{UP_{SPD}}$ ( $\text{m s}^{-1}$ )	$\overline{UP_{DIR}}$ ( $^\circ$ )
15 JUL	2	3	66.0	17.0	60
<b>24 JUL</b>	2	2/3	27.5	4.5	35
25 JUL	1	3	90.0	13.5	119
<b>26 JUL</b>	3	3	96.7	8.5	120
<b>27 JUL</b>	2	2	40.0	7.0	95
<b>2 AUG</b>	3	2	88.3	4.5	115
5 AUG	5	3	98.0	7.0	114
9 AUG	4	3	63.8	10.0	115
10 AUG	3	2/3	70.0	6.0	105
<b>13 AUG</b>	2	3	90.0	9.0	100
<b>15 AUG</b>	5	3	99.0	7.0	130

In the data processing, contamination from ground clutter and second trip echos were removed. Doppler velocity data were dealiased. Afterwards, data measured at the  $0.3^\circ$  elevation angle with range resolution of about 150 m were interpolated from a spherical onto a Cartesian coordinate system located at a height of 0.3 km above ground level (AGL) having a horizontal resolution of 600 m using NCAR's REORDER software (Oye and Case 1995). Deriving grid points, a Cressmann distance dependent weighting scheme was applied (Cressmann 1959). After the spacial interpolation, a multiple-Doppler radar wind synthesis using the method of least-squares are applied to derive the horizontal wind fields from the measured radial Doppler velocities. Wind synthesis was performed using

NCAR's CEDRIC software package (Mohr et al. 1986).

### 3. ANALYSIS PERFORMANCE

#### a Intensity and Distribution of Kinematic Structures

The investigation concentrated on kinematic structures behind, within, and ahead of the gust-fronts observed during CaPE. Observational times chosen for this investigation represent the late mature stage of gust fronts that both were disjointed completely from the thunderstorms and did not interact with approaching sea-breezes. In all cases, gust fronts propagated with a speed between 5 and  $17 \text{ m s}^{-1}$  eastwards (Tab. 1). The analysis of kinematic structures was performed within a coordinate system having the main axes parallel and orthogonal to the guest front. In doing so, the Cartesian coordinate system consisting of a northward distance  $y$  and an eastward distance  $x$  was rotated to a system with the  $y'$ -axis parallel and the  $x'$ -axis orthogonal to the guest front. In order to meet this condition, each gust front was usually divided into different segments which were then rotated individually. An example is given in Fig. 2 illustrating the thunderstorm together with the gust front on the west side and the sea-breeze front on the east side of the observation domain. Fig. 2a portrays the normal meteorological coordinate system oriented in south-north and west-east direction. For further analysis of this case, the coordinate system was then rotated anticlockwise by both  $30^\circ$  (Fig. 2b) and  $12^\circ$  (Fig. 2c), respectively, in order to orient the northern and southern gust-front segment parallel to the  $y'$  axis.

The investigation on mesocyclone development focused on three parts: (1) the analysis of temporally and spatially averaged vertical vorticity and convergence at low-levels within the gust front; (2) the spatial progress of the wind components parallel and orthogonal to the gust front; and (3) the impact of the pre- and post-frontal wind conditions in relation to mesocyclone development. All calculations based solely on the horizontal wind vector,  $\mathbf{V}_h$ , derived from Doppler radar measurements.

For part (1) and part (3), the investigation was carried out within a boxed region according to the length of each segment (length refers to  $y'$  extension). The frontal region was defined as having a width of about  $6 \text{ km}^1$  centered around the convergence wind line observable also as thin line of enhanced reflectivity ranging between 0 and  $20 \text{ dBZ}_e$  (cf. middle boxes in Figs. 2b and c including the  $10 \text{ dBZ}_e$  contour lines). The identification of the frontal zone was based solely on radar signatures of enhanced reflectivity lines together with lines of enhanced convergence, vorticity signatures and a change of wind speed and direction. The gust fronts had a length larger than 10 km and were present for a minimum of 15 minutes. The average length of the analyzed gust fronts ranged between 40–100 km ( $\Delta y'$  in Tab. 1). Post-frontal was defined as the area behind the gust front region, while pre-frontal covers the area ahead of the gust fronts' leading edge relative to the direction of propagation. Both the pre- and post-frontal regions having a width of 12 km (width refers to  $x'$  extension) adjoined the frontal zone. The box size was only minimized when either large parts of

<sup>1</sup>Based on data derived from radar measurements and mesonet stations, Wilson and Schreiber (1986) referred to a convergence zone width ranging between 0.5 and 5 km.

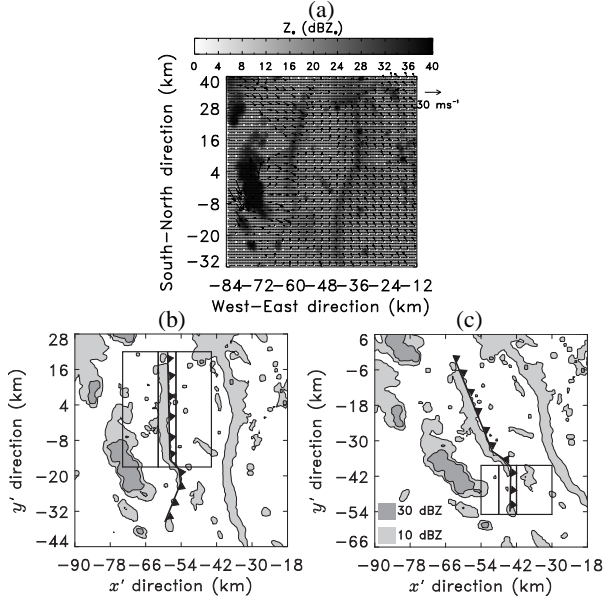


FIG. 2: Analysis of kinematic structures behind, within, and ahead of the gust front. (a) Horizontal wind field ( $\text{m s}^{-1}$ ; arrows) overlaid by reflectivity factor field (dBZ) measured at 2238 UTC on 13 August 1991. Data were sampled by CP3, CP4, and FL2 radar systems. For clarity of display, the wind vectors are plotted with a horizontal resolution of 3 km. (b) As (a) but coordinate system is rotated anticlockwise by  $30^\circ$ . Areas containing 3- or 35-dBZ reflectivity factors are illustrated, respectively. (c) As (a) but rotated anticlockwise by  $12^\circ$  highlighting the 10- or 35 dBZ reflectivity values. Analysis focuses on the post-frontal gust front area (left box), within the gust front itself (middle box), and the pre-frontal area (right box). Distances labeled at the coordinate axis are related to the position of CP4 located at (0,0).

the thunderstorm or the sea-breeze front itself occurred in the 12-km box as applied for instance for the post-frontal box at 2238 UTC on 13 Aug 1991 (Fig. 2c). Additionally those data points were not considered for the post-frontal-area analysis where the reflectivity value exceeds  $30 \text{ dBZ}_e$  (Fig. 2b, south-west corner of post-frontal box).

In order to investigate misocyclone development along the frontal zone, the maximum and the averaged maximum vertical vorticity,  $\zeta_{\max}$ ,  $\bar{\zeta}_{\max}$ , and the minimum and the averaged minimum divergence,  $(\nabla \cdot \mathbf{V}_h)_{\min}$ ,  $(\bar{\nabla} \cdot \mathbf{V}_h)_{\min}$ , were evaluated within the gust-front region (middle boxes in Figs. 2b and c) for each event. The results of the daily averages are listed in Tab. 2.

In part (2), both  $u'$ - and  $v'$ -component velocities were averaged along each  $x'$  cross-section. For each cross-section, averaging was assigned to the  $u'$ 's maximum gradient in  $x'$  direction or the  $v'$ 's absolute minimum value, respectively. An example of the averaged  $u'$ - and  $v'$ -component velocities along  $x'$  is given in Fig. 3 for measurements taken at 2234 UTC on 13 August 1991. Note that the maximum of  $\partial u' / \partial x$  and the minimum of  $v'$  are located at  $x' = 0 \text{ km}$ , respectively.

The averaged pre- and post-frontal  $u'$  components,

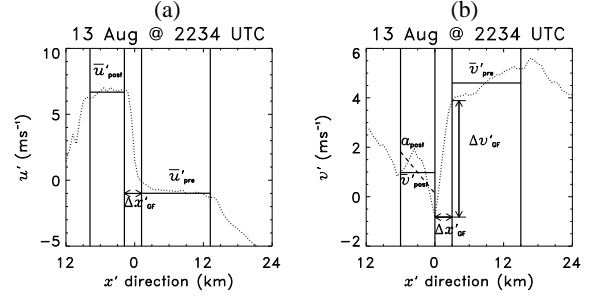


FIG. 3: Cross-section perpendicular to the gust front of the averaged (a)  $u'$  and (b)  $v'$  wind component measured at 2238 UTC on 13 August 1991. For each case the gust front width,  $\Delta x'_{\text{GF}}$ , the average post- and pre-frontal wind velocities,  $\bar{u}'_{\text{post}}$ ,  $\bar{u}'_{\text{pre}}$ ,  $\bar{v}'_{\text{post}}$  and  $\bar{v}'_{\text{pre}}$ , respectively, are evaluated. For the  $v'$  component, the post-frontal  $v'$ -slope,  $\alpha_{\text{post}}$ , and the  $v'$  difference,  $\Delta v'_{\text{GF}}$ , are additionally calculated.

$\bar{u}'_{\text{pre}}$  and  $\bar{u}'_{\text{post}}$ , were analyzed as illustrated in Fig. 3a in order to quantify the low-level divergence along the gust-front. The gust front area itself was hypothesized as the area with a gradient of  $\partial u' / \partial x'$  larger than  $0.2 \text{ m s}^{-1}$  around  $x' = 0$ . This threshold was chosen empirically based on the average shape of  $u'$  for all cases. Nevertheless, since the width of the gust front region should not exceed a value of 6 km, the threshold-derived gust front boundaries had to be varied slightly in some cases. At 2234 UTC on 13 August 1991, the gust front, however, was within  $-3 \text{ km} \leq x' \leq 2 \text{ km}$  as illustrated by  $\Delta x'_{\text{GF}}$  in Fig. 3. Based on these boundaries, the post-frontal area was defined generally 12 km behind of the tail of the gust front, while pre-frontal was 12 km ahead of the leading edge of the gust front. The average velocity values,  $\bar{u}'_{\text{pre}}$  and  $\bar{u}'_{\text{post}}$  were calculated within these areas. Again, only when either large parts of the thunderstorm or the sea-breeze front itself occurred in the 12-km box, the 12-km box width was reduced (cp. the post-frontal region in Figs. 2b, c, and Fig. 3a).

Table 2: Characteristics of kinematic structures presented as daily averages within the boxed region including the gust fronts: average maximum vorticity,  $\bar{\zeta}_{\max}$ , maximum vorticity,  $\zeta_{\max}$ , average maximum convergence,  $\bar{\nabla} \cdot \mathbf{V}_{h,\max}$ , and maximum convergence  $\nabla \cdot \mathbf{V}_{h,\max}$ .

Date	$\bar{\zeta}_{\max}$ $\times 10^{-3}$	$\zeta_{\max}$ $\text{s}^{-1}$	$\bar{\nabla} \cdot \mathbf{V}_{h,\max}$ $\times 10^{-3}$	$\nabla \cdot \mathbf{V}_{h,\max}$ $\text{s}^{-1}$
15 JUL	4.35	13.88	4.67	11.65
24 JUL	2.71	5.67	3.96	5.34
13 AUG	2.45	6.41	3.21	6.18
26 JUL	1.65	5.30	3.17	4.90
27 JUL	1.53	3.95	1.76	4.55
9 AUG	1.47	5.52	2.07	4.73
15 AUG	1.42	4.12	2.38	4.34
5 AUG	1.10	3.43	1.17	3.86
10 AUG	1.03	2.77	1.70	3.12
2 AUG	0.94	2.95	1.02	2.55
25 JUL	0.69	2.75	2.24	4.45

The approach for the  $v'$  component is similar than for the  $u'$  component. The gust front tail is located at  $x' = 0$ , the leading edge as  $\partial v'/\partial x' \leq xxxs^{-1}$ . Post- and pre-frontal is defined in the same way as for the  $u'$  component. Additionally to the above-discussed parameters, a linear fit is applied to the velocities within the post-frontal box (thick, dotted line post-frontal region in Fig. 3b) in order to quantify the anti-cyclonic shear behind the gust front. Again,  $\bar{v}'_{\text{post}}$  and  $\bar{v}'_{\text{pre}}$ , together with the differences,  $\Delta v'_{\text{GF}}$  within the threshold-defined gust front area, and the anti-cyclonic shear expressed by the slope,  $a_{\text{post}}$ , were calculated (results are listed in Table 3). An illustration of the analyzed parameters for the  $v'$  component is given in Fig. 3b.

To investigate the impact of the pre- and post-frontal wind conditions in relation to the misocyclone development (denoted as part 3), the averaged pre- and post-frontal wind velocities and directions were calculated within the pre- and post-frontal boxes, respectively.

#### b Convection initiation

In the third analysis step we determined weather or not there was an apparent causal relationship between misocyclone development along gust fronts and initiation of convection. The analysis of convection initiation focused on newly-developed precipitation areas that have a reflectivity core higher than 30 dBZ<sub>e</sub> and were not attached to already existing storms. Convective cell initiation was monitored after the gust front passage. When a single cell evolved into a multicellular storm it was classified as a single storm. Note that the investigation concentrated solely on the time period before gust fronts collided with the sea-breeze front. The analysis based on reflectivity factor measurements achieved by the C-band Doppler radar CP4. Since drops larger than a few hundred microns in diameter can only be detected by radars with a transmitting wavelength between 10–3 cm, it cannot be distinguished weather convection was initiated by convergence-line-related kinematic features or if the depth of existing clouds was intensified after the boundary passed.

## 4. DISCUSSION

A clear link between misocyclone development and convection initiation was not found in the cases observed during the CaPE experiment. Those parameters quantifying the strength of misocyclones along the gust-fronts are displayed in Tabs. 2, 3, and Fig. 4. Note that the dates in Tabs. 2, 3 and Figs. 4, 5 are sorted according to the maximum average vertical vorticity. While the 15-July-case showed by far the strongest misocyclone development, only on 24 Jul and 13 Aug strong misocyclones were observed with average maximum vorticities ranging between  $1.5\text{--}4 \times 10^{-3} \text{ s}^{-1}$ . Weak misocyclone development ( $\bar{\zeta}_{\text{max}} \leq 1 \times 10^{-3} \text{ s}^{-1}$ ) was observed on 5 Aug, 10 Aug, 2 Aug, and 25 Jul (Tab. 2).

Only the three strongest cases showed a strong signal in the spatial progress of  $v'$  (Fig. 4): Post-frontal the wind blow mainly perpendicular to the gust front with an average velocity ranging between  $-0.26$  and  $0.73 \text{ m s}^{-1}$  ( $\bar{v}'_{\text{post}}$  in Tab. 3). Note the wind analysis within the post-frontal box for the 24-Jul-case is limited because convective cells were located only

Table 3: Distribution of the wind component parallel and orthogonal to the gust front,  $v'$  and  $u'$  along the gust front. The analysis includes averaged post- and pre-frontal velocities,  $\bar{v}'_{\text{post}}$ ,  $\bar{v}'_{\text{pre}}$ ,  $\bar{u}'_{\text{post}}$ , and  $\bar{u}'_{\text{pre}}$ , respectively; their differences,  $\bar{v}'_{\text{post-pre}}$  and  $\bar{u}'_{\text{post-pre}}$ ; the linear fit of post-frontal  $v'$ ,  $a_{\text{post}}$ , and the velocity difference within the gust front area  $\Delta v'_{\text{GF}}$ . Cases with convective cell initiation after the gust front passage are highlighted in bold.

Date	$\bar{v}'_{\text{post}}$ m s <sup>-1</sup>	$\bar{v}'_{\text{pre-post}}$ m s <sup>-1</sup>	$a_{\text{post}}$ m s <sup>-1</sup> km	$\Delta v'_{\text{GF}}$ m s <sup>-1</sup>	$\bar{u}'_{\text{post}}$ m s <sup>-1</sup>	$\bar{u}'_{\text{pre}}$ m s <sup>-1</sup>	$\bar{u}'_{\text{post-pre}}$ m s <sup>-1</sup>
15 JUL	-0.26	6.18	-2.80	9.86	17.18	1.07	
<b>24 JUL</b>	<b>-4.36</b>	<b>7.94</b>	<b>0.65</b>	<b>6.45</b>	<b>13.48</b>	<b>0.69</b>	
<b>13 AUG</b>	<b>0.73</b>	<b>4.11</b>	<b>-0.31</b>	<b>5.28</b>	<b>6.70</b>	<b>-1.00</b>	
<b>26 JUL</b>	<b>2.27</b>	<b>0.58</b>	<b>-0.54</b>	<b>2.59</b>	<b>9.52</b>	<b>-0.41</b>	
<b>27 JUL</b>	<b>0.17</b>	<b>2.05</b>	<b>-0.28</b>	<b>3.20</b>	<b>4.29</b>	<b>-0.85</b>	
9 AUG	-1.63	0.99	-0.48	2.71	9.25	4.22	
<b>15 AUG</b>	<b>0.71</b>	<b>1.98</b>	<b>-0.10</b>	<b>3.36</b>	<b>7.40</b>	<b>0.74</b>	
5 AUG	-0.79	3.00	0.06	2.96	4.48	2.87	
10 AUG	2.32	1.47	-0.08	1.74	3.52	-1.39	
<b>2 AUG</b>	<b>1.47</b>	<b>2.09</b>	<b>-0.03</b>	<b>1.73</b>	<b>5.14</b>	<b>1.25</b>	
25 JUL	-0.94	0.90	-0.19	0.86	7.86	1.74	

3 km behind the gust front. Hence, the analysis areas was reduced by about 75% compared to 15 Jul and 13 Aug. Considering the progress of  $v'$ , the component orthogonal to the gust front increases up to  $8 \text{ m s}^{-1}$  for 24 Jul;  $6 \text{ m s}^{-1}$  for 15 Jul; and  $4 \text{ m s}^{-1}$  for 13 Aug (Fig. 4 upper panel,  $\bar{v}'_{\text{pre-post}}$  in Tab. 3). In those weaker cases, where the wind velocity differences,  $\bar{v}'_{\text{pre-post}}$  were about  $2\text{--}3 \text{ m s}^{-1}$  (27 Jul, 15 Aug, 5 Aug, 2 Aug), the post-frontal  $v'$ -component ranged between  $\pm 1.5 \text{ m s}^{-1}$  (Fig. 4, Tab. 3). Nevertheless, one can observe a pronounced anticyclonic shear effect, displayed by a rapid loss of the  $v'$  as illustrated for 15 Jul and 13 Aug in Fig. 4. Anticyclonic shear along the gust front is less pronounced but still visible on 27 Jul, 5 Aug, and 15 Aug (Fig. 4). The strength of anticyclonic shear is expressed by the linear fit of  $v'$  in the post-frontal area and is visible as velocity drop few kilometers before the minimum value in Fig. 4. The fitted linear function decreased mainly with rates of  $a_{\text{post}}$  ranging between  $-0.3$  to  $-2.8 \text{ m s}^{-1} \text{ km}$  for the strong and medium cases. Again the strongest anti-cyclonic shear was observed on 15 Jul. In some weaker cases (26 Jul, 9 Aug, 10 Aug, and 25 Jul), however, the  $v'$  component stayed at the same level in the pre- and post-frontal region (Fig. 4, Tab. 3). Note, again the post-frontal region on 24 Jul cannot be analyzed.

The average convergence for the cases with strong and medium misocyclone development range between about  $2$  to  $4 \times 10^{-3} \text{ s}^{-1}$ , while the local minimum values of  $(\nabla \cdot \mathbf{V}_h)_{\text{min}}$  in the cases with strong misocyclone development (15 Jul, 24 Jul, 13 Aug) are much lower with values between  $-6$  and  $-12 \times 10^{-3} \text{ s}^{-1}$  (Tab. 2). Again, the 15-Jul-case showed both the highest average and local value in convergence. In the analysis of the velocity component parallel to the gust front,  $u'$ , one is interested in the relative velocity decrease post- and pre-frontal. Interestingly, no strong shear with high positive values post-frontal and high negative values pre-frontal

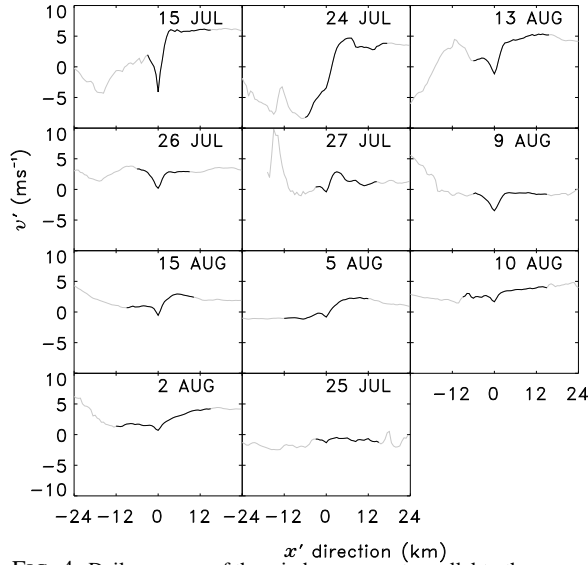


FIG. 4: Daily average of the wind component parallel to the boundary. The dark black line represents the area where the statistical analysis was applied.

are visible (Tab. 3). Almost all cases have a pre-frontal  $u'$ -component velocity ranging between  $\pm 1 \text{ m s}^{-1}$ . Nevertheless, huge differences occurred the post-frontal  $u'$ -component velocity. Again, high differences were observed for cases with strong and medium misocyclone development (15 Jul, 24 Jul, 13 Aug, 26 Jul, 15 Aug) with values of  $\bar{u}'_{\text{post-pre}}$  ranging between 5 and  $16 \text{ m s}^{-1}$  (Fig. 5, Tab. 3). Low convergence with relatively high vertical velocity was observed on 27 Jul and 8 Aug.

The analysis of the pre- and post-frontal wind velocity calculated within the rotated coordinate system makes clear, that both on 25 Jul and 9 Aug the wind shift (less than  $60^\circ$ ) was too weak to develop strong divergence and strong vertical velocities leading to no convection development (Figure not shown). The shift in wind direction is the determining factor for the development of strong convergence and vertical vorticity zones.

For the eleven cases to be investigated only six out of eleven (55%) showed convective initiation related to low-level gust fronts. No convective initiation was observed on 15 Jul, 25 Jul, 5 Aug, 9 Aug, and 10 Aug 1991. Note that all cases with convection initiation after the boundary passed are marked as bold text. Beside wind shear features, the strength and development of thunderstorms depend on the static stability of the environment. Fig. 6 shows the relationship between the convective available potential energy, CAPE, the divergence, and the lifted index. CAPE and lifted index were derived from radiosoundings launched either in Orlando or Deer Park (see Fig. 1) depending on the location of the gust front. On 25 Jul and 5 Aug, the environmental conditions within the area where the gust fronts passed were not favored to produce any convection (Fig. 6a). While on 10 Aug CAPE was very high, the average divergence was too low to initiate convection.

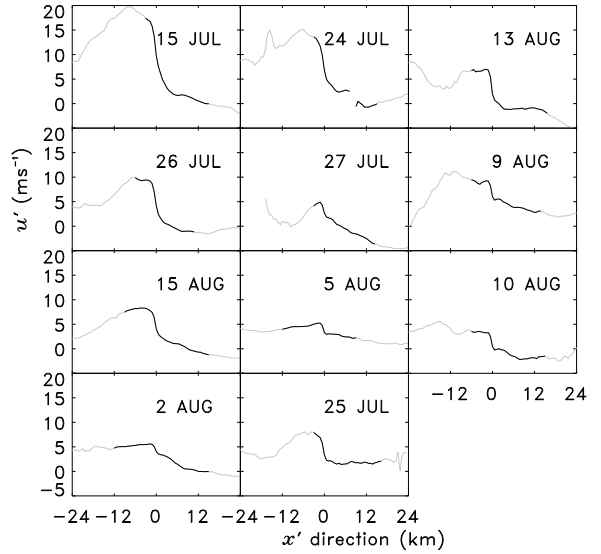


FIG. 5: As Fig. 4, but for the wind component orthogonal to the boundary.

## 5. CONCLUSION

The investigation on a relation between misocyclone development and convection initiation so far yield to the conclusion that misocyclone development can yield to convection initiation but is not a basic requirement as shown on 15 Jul 1991. The linkage between misocyclone development, strength of convergence, wind shear, and CAPE are summarized in Tab. 4.

The investigations yield to the general conclusions:

- (1) Convection initiation depend mainly on static stability and wind shear, i.e. although CAPE values, the average convergence and vertical vorticities values were in fact sufficient to develop convection on 9 Aug, the shear in wind direction pre- and post-frontal was too weak to trigger the initiation. No favoured environmental conditions for convection development ( $\text{CAPE} > 300 \text{ J kg}^{-1}$ ) were found on 5 Aug, 25 Jul.

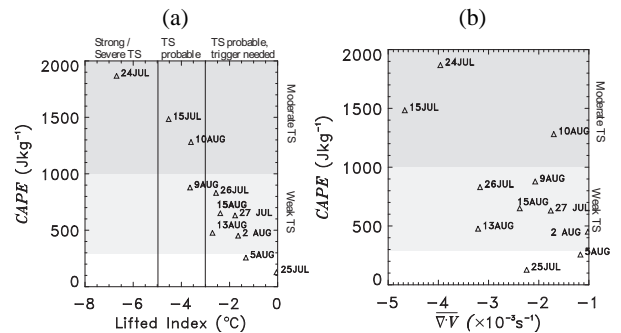


FIG. 6: Convective available potential energy (CAPE) as a function of (a) the lifted index and (b) the averaged divergence for the eleven analyzed cases. CAPE and lifted index were derived from the radiosounding launched at the temporally and spatially closest point according to the gust front location and time. Divergence was derived from the Doppler wind information measured by the radar network.

Table 4: Summary of the cases analyzed from the CaPE experiment, marking the appearance of strong kinematic features like misocyclone development, convergence, and wind shear together with stability parameter CAPE.

Date	$\zeta_{\max}$	$(\nabla \cdot \mathbf{V}_h)_{\min}$	$\text{dir}'_{\text{post-pre}}$	CAPE
15 JUL	x	x	x	x
<b>24 JUL</b>	x	x	x	x
<b>13 AUG</b>	x	x	x	x
<b>26 JUL</b>	x	x	x	x
<b>27 JUL</b>	x		x	x
9 AUG	x			x
<b>15 AUG</b>	x	x	x	x
5 AUG			x	
10 AUG			x	x
<b>2 AUG</b>			x	x
25 AUG		x		

- (1) A positive linkage between misocyclone development and convection initiation was found for five cases (45.5%). A negative linkage, however, i.e. convection initiated although no strong misocyclones developed (2Aug), or strong micocyclones developed but no convection (15 Jul, 9 Aug) was investigated in 27% of the cases.
- (2) Wind shear and CAPE are directly linked to convective initiation, i.e. if wind shear and CAPE are too low no convection is initiated as on 9 Aug, 5 Aug, 25 Jul. Contrary to that, no convection developed on 10 Aug, although wind shear and CAPE were favoured.
- (3) outliers are 15 Jul, 10 Aug, 2 Aug
- (4) According to (Lee and Wilhelmson 1997), misocyclone development is a strengthening factor

As a result, convection initiation depend on several parameters. Misocyclone development is one main parameter that can trigger or enhance convection together with stability parameters. The linkage between misocyclone development and convective initiation does exist as shown by (Lee and Wilhelmson 1997) and certainly 'play a significant role in deep convection initiation'. On the other hand, this investigations shows that the results achieved from numerical models can be certainly found in nature but do not represent the structure along an outflow boundary. Further statistical analysis will show, if the eleven cases are representativ.

## REFERENCES

- Atkins, N. T., R. M. Wakimoto, and T. M. Weckwerth, 1995: Observations of the sea-breeze front during cape. part ii: Dual-doppler and aircraft analysis. *Mon. Wea. Rev.*, **123**, 944–969.
- Cooper, H. J., M. Garstang, and J. Simpson, 1982: The diurnal interaction between convection and peninsula-scale forcing over south florida. *Mon. Wea. Rev.*, **110**, 486–503.
- Cressmann, G. P., 1959: An operational objective analysis system. *Mon. Wea. Rev.*, **87**, 367–374.
- Frankhauser, J. C., N. A. Crook, J. Tuttle, L. J. Miller, and C. G. Wade, 1995: Initiation of deep convection along boundary layer convergence lines in a semitropical environment. *Mon. Wea. Rev.*, **123**, 291–313.
- Fujita, T. T., 1981: Tornadoes downbursts in the context of generalized planetary scales. *J. Atmos. Sci.*, **38**, 1511–1534.
- Kingsmill, D. E., 1995: Convection initiation associated with a sea-breeze front, a gust front, and their collision. *Mon. Wea. Rev.*, **123**, 2913–2933.
- Kingsmill, D. E. and N. A. Crook, 2003: An observational study of atmospheric bore formation from colliding density currents. *Mon. Wea. Rev.*, **131**, 2985–3002.
- Laird, N. F., D. A. R. Kristovich, R. M. Rauber, H. T. Ochs, and L. J. Miller, 1995: The cape canaveral sea and river breezes: Kinematic structure and convective initiation. *Mon. Wea. Rev.*, **123**, 2942–2956.
- Lee, B. D. and R. B. Wilhelmson, 1997: The numerical simulation of non-supercell tornadogenesis. part i: Initiation and evolution of pretornadic misocyclone circulation along a dry outflow boundary. *J. Atmos. Sci.*, **54**, 32–60.
- Mohr, C. G., L. Miller, R. Vaughan, and H. Frank, 1986: The merger of mesoscale datasets into a common cartesian format for efficient and systematic analysis. *J. Atmos. Oceanic Technol.*, **3**, 143–161.
- Oye, D. and M. Case, 1995: *REORDER-A program for gridding radar data. Installation and use manual for the Unix version.* Research Data Program, Atmospheric Technology Division, National Center for Atmospheric Research, Available online at <http://www.atd.ncar.edu/rsf/uuserGuides/ELDORA/dataAmalysis/reorder/tu>
- Purdom, J. F. W. and K. Marcus: 1982, Thunderstorm trigger mechanisms over the southeast u.s. *Proc. 12th Conf. on Severe Local Storms, San Antonio*, Amer. Meteor. Soc., 487–488.
- Wakimoto, R. M. and D. E. Kingsmill, 1995: Structure of an atmospheric undular bore generated from colliding boundaries during cape. *Mon. Wea. Rev.*, **123**, 1374–1393.
- Watson, A. I. and D. O. Blanchard, 1984: The relationship between total area divergence and convective precipitation in south florida. *Mon. Wea. Rev.*, **112**, 673–685.
- Wilson, J. W. and W. E. Schreiber, 1986: Initiation of convective storms at radar-observed boundary-layer convergence lines. *Mon. Wea. Rev.*, **114**, 2516–2536.
- Yuter, S. E. and R. A. Houze, 1995: Three-dimensional kinematic and microphysical evolution of florida cumulonimbus. part i: Spatial distribution of updraft, downdraft, and precipitation. *Mon. Wea. Rev.*, **123**, 1921–1940.